AGU PUBLICATIONS

JGR

Journal of Geophysical Research: Solid Earth

RESEARCH ARTICLE
10.1002/2015JB011914

Key Points:
- Ten percent of clay in water-saturated calcite gouges can facilitate surface faulting
- It also inhibits the development of microstructures associated with seismic slip
- The weakness of wet clay-bearing gouges is explained via a microphysical model

Supporting Information:
- Texts S1–S7

Correspondence to:
R. J. Bullock,
r.j.bullock@durham.ac.uk

Citation:
Bullock, R. J., N. De Paola, and R. E. Holdsworth (2015), An experimental investigation into the role of phyllosilicate content on earthquake propagation during seismic slip in carbonate faults, *J. Geophys. Res. Solid Earth*, *120*, doi:10.1002/2015JB011914.

Received 5 FEB 2015
Accepted 29 APR 2015
Accepted article online 4 MAY 2015

An experimental investigation into the role of phyllosilicate content on earthquake propagation during seismic slip in carbonate faults

Rachael J. Bullock[1], Nicola De Paola[1], and Robert E. Holdsworth[1]

[1]Rock Mechanics Laboratory, Department of Earth Sciences, University of Durham, Durham, UK

Abstract Carbonate faults commonly contain small amounts of phyllosilicate in their slip zones, due to pressure solution and/or clay smear. To assess the effect of phyllosilicate content on earthquake propagation in carbonate faults, friction experiments were performed at 1.3 m/s on end-members and mixtures of calcite, illite-smectite, and smectite gouge. Experiments were performed at 9 MPa normal load, under room humidity and water-saturated conditions. All dry gouges show initial friction values (μ_i) of 0.51–0.58, followed by slip hardening to peak values of 0.61–0.76. Slip weakening then ensues, with friction decreasing to steady state values (μ_{ss}) of 0.19–0.33 within 0.17–0.58 m of slip. Contrastingly, wet gouges containing 10–50 wt % phyllosilicate exhibit μ_i values between 0.07 and 0.52 followed by negligible or no slip hardening; rather, steady state sliding ($\mu_{ss} \ll 0.2$) is attained almost immediately. Microstructurally, dry gouges show intense cataclasis and wear within localized principal slip zones, plus evidence for thermal decomposition of calcite. Wet gouges exhibit distributed deformation, less intense cataclasis, and no evidence of thermal decomposition. It is proposed that in wet gouges, slip is distributed across a network of weak phyllosilicate formed during axial loading compaction prior to shear. This explains the (1) subdued cataclasis and associated lack of slip hardening, (2) distributed nature of deformation, and (3) lack of evidence for thermal decomposition, due to low friction and lack of slip localization. These findings imply that just 10% phyllosilicate in the slip zone of fluid-saturated carbonate faults can (1) dramatically change their frictional behavior, facilitating rupture propagation to the surface, and (2) significantly lower frictional heating, preventing development of microscale seismic markers.

1. Introduction

Phyllosilicates are traditionally viewed as having a stabilizing influence on the behavior of upper crustal fault zones. Experimental studies have shown that most phyllosilicates behave in a predominantly velocity-strengthening manner when deformed at subseismic slip rates (<1 cm/s) [*Saffer and Marone*, 2003; *Ikari et al.*, 2009; *Tembe et al.*, 2010; *Moore and Lockner*, 2011; *Behnsen and Faulkner*, 2012; *Sone et al.*, 2012; *Tesei et al.*, 2012]. Therefore, earthquakes are unable to nucleate in upper crustal fault zones that are rich in phyllosilicates. Instead, phyllosilicate-rich fault zones are widely believed to deform predominantly aseismically by fault creep [*Marone*, 1998; *Scholz*, 1998]. For example, the creeping behavior of the Parkfield segment of the San Andreas Fault is attributed to the presence of smectitic phyllosilicates in fault gouges [e.g., *Carpenter et al.*, 2011; *Holdsworth et al.*, 2011; *Lockner et al.*, 2011]. In addition, crustal regions containing a significant proportion of such velocity-strengthening materials, such as poorly lithified, clay-rich fault gouges, are viewed as energy sinks, due to a negative stress drop, with the potential to attenuate, or even arrest, an earthquake rupture as it propagates toward the surface [*Scholz*, 1998].

The frictional behavior of phyllosilicates at seismic slip rates is quite different to that observed at subseismic slip rates. When subject to slip velocities in excess of 1 cm/s, phyllosilicates can undergo dynamic weakening; after attaining a peak in friction at the onset of slip, they undergo an exponential decay in frictional strength, of up to 90% [e.g., *Boutareaud et al.*, 2008; *Brantut et al.*, 2008; *Ferri et al.*, 2010; *Ujiie and Tsutsumi*, 2010; *Faulkner et al.*, 2011]. This is a phenomenon observed for a wide range of rock types and has been attributed to mechanically and thermally activated reactions which weaken the fault during fast, localized slip [see *Di Toro et al.*, 2011].

Wet phyllosilicates subject to seismic slip again show a different frictional behavior; they do not attain a peak in friction and instead attain steady state sliding immediately at the onset of slip [*Ferri et al*., 2010; *Ujiie and Tsutsumi*, 2010; *Faulkner et al*., 2011; *Ferri et al*., 2011; *Ujiie et al*., 2011, 2013]. These results from high-velocity friction experiments suggest that particularly when wet, velocity-strengthening phyllosilicates may offer less resistance to seismic slip than other rock types, provided that dynamic stresses continue to produce a large enough velocity jump to trigger dynamic weakening. The reasons saturated clay-rich gouges are so weak when subject to seismic slip velocities are not well understood. Suggestions have included rapid thermal pressurization at the onset of slip [*Faulkner et al*., 2011] and pore fluid pressurization due to a combination of shear-enhanced compaction and frictional heating [*Ujiie and Tsutsumi*, 2010]. Alternatively, *Ferri et al*. [2010] proposed that the low friction coefficients associated with water-saturated clays may be due either to water molecules bonding to the surfaces of clay grains, forming thin, lubricating films (as per *Moore and Lockner* [2004]), or to water being extruded from the gouge layer during compaction and localizing at the gouge-wall rock interface so that friction is controlled by a lubricating film of water. However, these theories lack robust experimental evidence.

The complex range of frictional behaviors observed in the lab presents us with the challenge of trying to understand what role phyllosilicates may play in the behavior of natural fault zones. Phyllosilicates are widely recognized to be prevalent within clay-rich fault gouges of upper crustal faults [e.g., *Wu et al*., 1975; *Vrolijk and van der Pluijm*, 1999; *Faulkner et al*., 2003; *Holdsworth*, 2004], and within accretionary wedges at subduction zones, which frequently host tsunamigenic earthquakes [e.g., *Lay et al*., 2005; *Ide et al*., 2011; *Chester et al*., 2013]. But they are also common constituents of carbonate fault zones, for example, if the protolith is a marly limestone, or a limestone formation with marl interbeds [e.g., *Gratier et al*., 2013; *Tesei et al*., 2013; *Bullock et al*., 2014]. Several recent studies have documented the influence of phyllosilicates on the architecture and frictional behavior of carbonate fault zones. These studies include examples of strike-slip faults, e.g., the active Vuache fault in the French Alps [*Gratier et al*., 2013]; thrust faults, e.g., within the exhumed Northern Apennines fold-thrust belt in Italy (Figure 1) [*Tesei et al*., 2013]; and normal faults, e.g., the active Gubbio fault in the Northern Apennines (Figure 1) [*Bullock et al*., 2014] and the active Clansayes fault system in the French Alps [*Gratier et al*., 2013]. These studies have concluded, through a combination of geological, laboratory, and seismological observations, that marl- or phyllosilicate-rich fault domains host predominantly distributed deformation and aseismic slip, while limestone-dominated fault domains tend to host localized, brittle deformation and seismic rupture. This is attributed to the fact that pressure solution processes, and associated creep, are more efficient in polymineralic marls than in monomineralic limestone [*Gratier et al*., 2013] and that the phyllosilicates present within marls are almost exclusively velocity strengthening [e.g., *Morrow et al*., 2007; *Tembe et al*., 2010; *Ikari et al*., 2011], whereas limestone, under certain conditions, can behave in an unstable, velocity-weakening manner [*Logan et al*., 1992; *Verberne et al*., 2010; *Collettini et al*., 2011; *Verberne et al*., 2014].

As well as being associated with zones of distributed deformation within carbonate faults, phyllosilicates are also observed to be concentrated within the principal slip zones (PSZs) of many carbonate faults (Figures 1b–1e; see also Text S1 in the supporting information) [*Collettini et al*., 2013; *Tesei et al*., 2013; *Bullock et al*., 2014]. These phyllosilicates may have become concentrated in the PSZs either by smearing of clay interbeds along the fault during slip or by pressure solution acting on the fault planes or within the slip zones, preferentially removing the soluble carbonate phases and leaving behind the insoluble phyllosilicates. The phyllosilicate content within the PSZs may be as high as 50%, and often these minerals form interconnected networks of strongly aligned grains oriented subparallel to the PSZs [e.g., *Bullock et al*., 2014, Figure 9a]. In many cases, there is evidence that the phyllosilicate-enriched carbonate PSZs have hosted past seismic events [*Collettini et al*., 2013; *Tesei et al*., 2013; *Bullock et al*., 2014]. The effect that phyllosilicate content may have on the frictional behavior of carbonate faults during seismic slip represents a subject of critical importance, particularly since earthquakes within the Italian Apennines, one of the most seismically active zones in Europe (Figure 1a) [e.g., *Lavecchia et al*., 2003; *D'Agostino et al*., 2009; *Chiaraluce*, 2012; *Ventura and Di Giovambattista*, 2013], all nucleate within and propagate through a carbonate multilayer sequence comprising interbedded limestones and marls [e.g., *Barchi et al*., 1998]. Thus, in order to assess the effect of variable phyllosilicate content on the frictional behavior of phyllosilicate-bearing carbonate faults during seismic slip, we present the results from a set of high-velocity friction experiments carried out on gouges containing different proportions of calcite and phyllosilicate, under dry and water-saturated

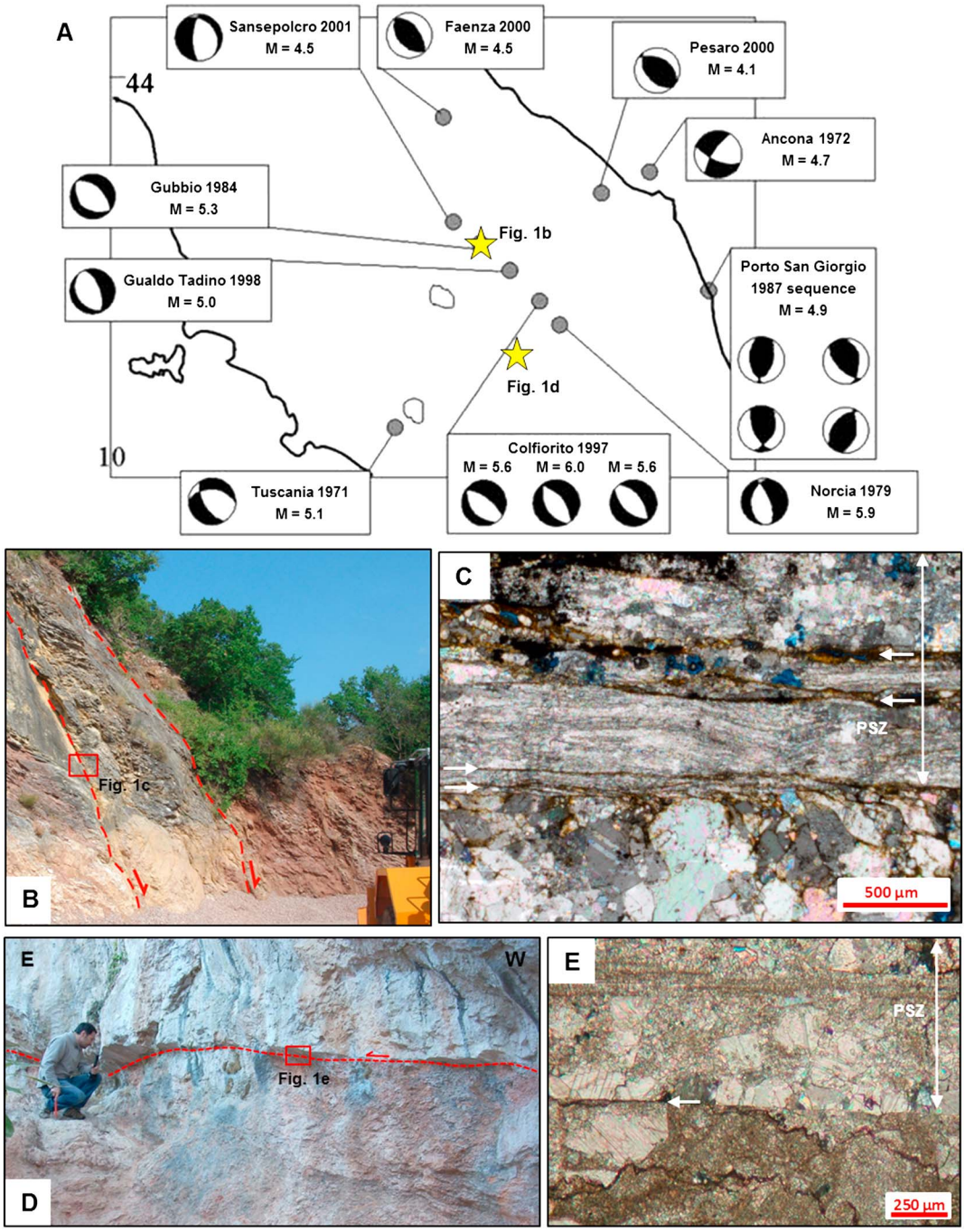

Figure 1. (a) Focal mechanism distribution within the Northern Apennines seismic belt in central Italy. Figure taken from *Collettini et al*. [2006]. (b) The active Gubbio normal fault (see Figure 1a for location), which deforms a mixture of Jurassic-Oligocene micritic limestone (yellow in color) and marly limestone (red in color). (c) Optical microscope image of a PSZ within the core of the Gubbio fault (see Figure 1b for sample location). The PSZ contains numerous slip surfaces (indicated by arrows), which are highlighted by the presence of dark brown phyllosilicate. The rest of the PSZ is dominated by calcite veining. Additional examples of phyllosilicate-enriched PSZs from the Northern Apennines are presented in Text S1. (d) The exhumed Spoleto thrust fault (see Figure 1a for location), which brings Lower Jurassic massive limestones in the HW on top of Cretaceous layered limestones in the FW. (e) Optical microscope image of the PSZ of the Spoleto fault (see Figure 1d for sample location). Again, the PSZ is dominated by calcite veining, and the PSS is contaminated by brown phyllosilicate (indicated by arrow) from pressure solution. Figures 1d and 1e are courtesy of Telemaco Tesei.

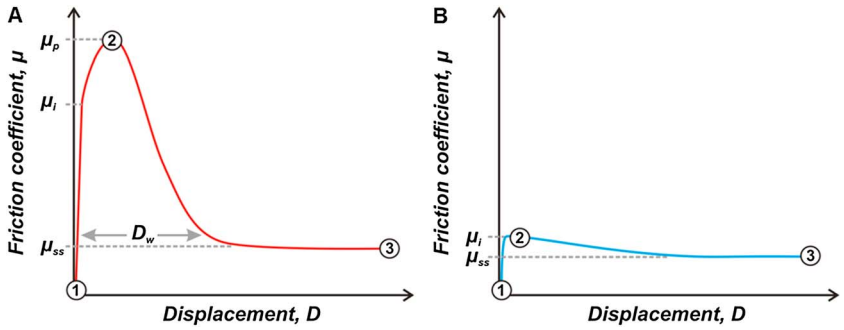

Figure 2. Schematic representation of frictional evolution during the experiments. (a) The case for gouges which exhibit a peak in friction during the experiments and (b) the case for gouges which do not exhibit a peak in friction. Numbering refers to the three stages at which samples were recovered for inspection. See text for explanation.

conditions. The mechanical data from our experiments are accompanied by microstructural observations of the deformed gouges, which we use to devise a micromechanical model that can be used to explain their frictional behavior.

2. Experimental Setup and Procedure

Friction experiments were performed using the Low to High Velocity Rotary Shear Apparatus at Durham University (Text S2). We deformed end-member gouges of calcite, mixed-layer illite-smectite, and smectite, as well as 50:50, 80:20, and 90:10 mixtures of calcite + illite-smectite and calcite + smectite. These are representative of the PSZ compositions observed in the Northern Apennines [*Collettini et al*., 2013; *Bullock et al*., 2014]. The calcite gouges were prepared from undeformed samples of the Scaglia Rossa limestone (~95% calcite), which were collected from field locations close to the exposure of the Gubbio fault [see *Bullock et al*., 2014]. The mixed-layer illite-smectite clay (90–98% purity) was obtained from the Clay Minerals Society Special Clays Repository, and the smectite was obtained as Na montmorillonite (90–100% purity) from the Clay Minerals Society Source Clays Repository. All samples were crushed by hand using a fly press and were subsequently ground to a fine powder using a pestle and mortar. These powders were then sieved to create synthetic gouges with a grain size range of 180–250 μm.

The samples were assembled for testing by sandwiching 1.5 g of gouge (or 1.2 g of gouge for wet experiments, to allow for volume increase when swelling clays were saturated) between two steel cylinders of 25 mm diameter. The surfaces of the steel cylinders are radially grooved to depths of 500 μm in order to ensure that slip localization occurs within the gouge layer rather than along the boundaries between the cylinders and the gouge. The gouge is confined by fixing a Teflon ring around the sample assembly [*Mizoguchi et al*., 2007] (Figure 2 of Text S2). The sample is then set within a vertical loading frame in which the lower cylinder remains stationary while the upper cylinder is rotated by a servomotor. An axial load is applied from the base of the loading frame via a pneumatic Bellofram cylinder. Friction during the experiments is measured using compression load cells attached to a high-precision arm-type torque meter, and output values were recorded by a data logger at a sampling frequency of 1 KHz.

Experiments were conducted at room temperature, and each sample was run both at room humidity ("dry") and under water-saturated ("wet") conditions. Prior to the room humidity experiments, the clays were oven dried overnight at 105°C to remove adsorbed water. For water-saturated experiments, ~0.27 mL of deionized water was applied to the gouge layer to achieve saturation. After application of normal load, samples were held for 3 min prior to shearing to allow for an initial phase of compaction. The experiments were then run at an equivalent velocity [*Shimamoto and Tsutsumi*, 1994] (Text S2) of 1.3 m/s, representative of seismic slip, and a normal load of 9 MPa (with the exception of experiment 416, which had to be run at 1.2 MPa due to the excessive mobilization of saturated montmorillonite gouge at higher normal loads).

Experiments were terminated at three different stages for sampling of deformed gouges. These stages were (Figure 2) (1) after application of normal load for 3 min, prior to shearing; (2) on attainment of peak friction, before slip weakening has occurred (or during the very early stages of slip in the case of gouges that do not

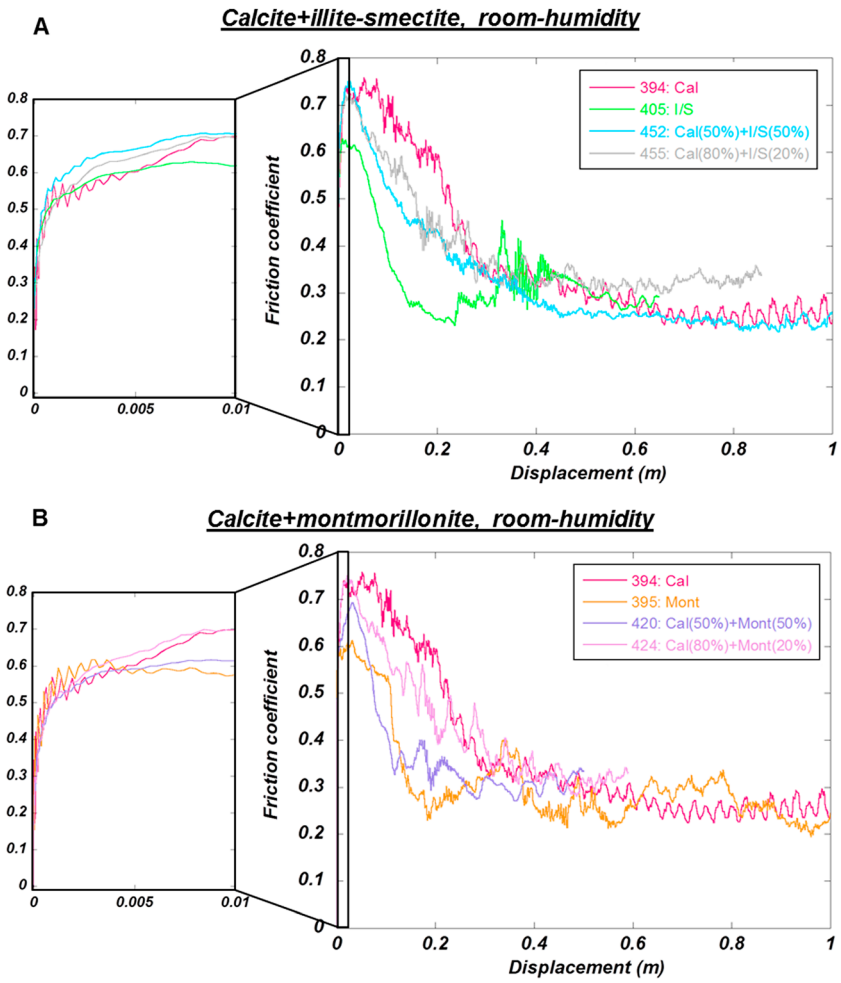

Figure 3. Experimental results for dry gouges sheared until the attainment of steady state sliding. The magnified section of the curve shows the initial slip-hardening phase during which the initial value of friction attained at the very start of the experiment increases toward a peak value. (a) Calcite and illite-smectite end-members and mixtures. (b) Calcite and montmorillonite end-members and mixtures.

exhibit a peak in friction); and (3) on attainment of steady state friction, subsequent to weakening. This systematic sampling enables observation of microstructural evolution during slip and an assessment of how grain- and aggregate-scale deformation mechanisms may influence frictional behavior.

The experimental configuration does not enable us to measure variations in pore fluid pressure, temperature, or gas emissions during our experiments. Therefore, in this manuscript we do not attempt to speculate on the dynamic weakening mechanisms that may be in operation during our experiments. We rely on microstructural observations of the deformed gouges to explain differences in mechanical behavior. In addition, since we cannot monitor pore pressure during the experiments, values of the friction coefficient are calculated as the measured shear stress divided by the applied normal load, rather than the effective normal stress. Our friction coefficient values may therefore be considered as apparent values, which neglect the effects of pore fluid pressurization due to decarbonation/dehydration reactions, shear heating of pore fluids, and compaction-driven pressurization. However, it is preferable to present the data in terms of friction coefficient, rather than shear stress, as it allows for easier comparison of data with previous studies, which have been performed at different normal loads. The inability to monitor pore fluid pressure is a common technical limitation during high-velocity friction experiments, which has only recently been overcome [*Violay et al.*, 2013]. Therefore, presenting our data in terms of apparent rather than true friction coefficient is in line with the majority of published results from high-velocity friction experiments.

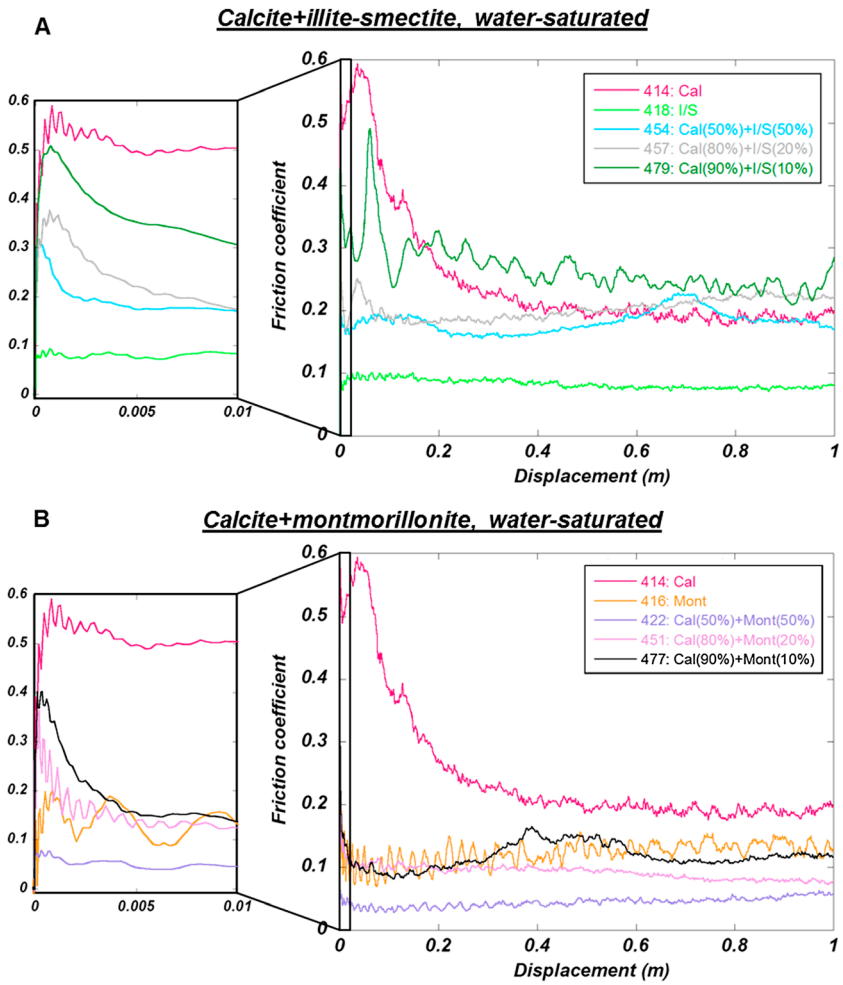

Figure 4. Experimental results for wet gouges sheared until the attainment of steady state sliding. The magnified section of the curve shows the initial slip-weakening phase during which the initial value of friction attained at the very start of the experiment decreases before either (1) restrengthening toward a peak value (in the case of experiments 414, 457, and 479) or (2) attaining steady state sliding without undergoing any slip hardening. (a) Calcite and illite-smectite end-members and mixtures. (b) Calcite and montmorillonite end-members and mixtures.

3. Results

3.1. Mechanical Data

3.1.1. Dry Gouges

Plots of friction coefficient against displacement for all experiments run until steady state are shown in Figures 3 and 4. These results are also summarized in Table 1 and Figure 5. Results of experiments terminated at peak friction are shown in Text S3. All of the experiments exhibit an initial phase of linear-elastic deformation prior to yielding. The yield point, at which the friction curve deviates from being linear, gives us the initial frictional strength of the gouge, μ_i (Figure 2; see also Text S4). For the dry end-member gouges, μ_i values are all similar, falling within the range 0.53–0.58 (Figures 3 and 5a). Within the first ~0.1 m of slip, μ_i is followed by a slip-hardening phase, during which friction evolves to a peak value, μ_p (Figure 3). The end-member calcite gouge has a μ_p value of 0.75 (Figures 3 and 5b), which is slightly higher than that of the clay end-members, which have μ_p values of 0.63 for illite-smectite (Figures 3a and 5b) and 0.61 for montmorillonite (Figures 3b and 5b). The peak in friction is followed by a dramatic decrease in frictional strength, over a slip-weakening distance, D_w, to steady-state values (μ_{ss}), which for all dry end-member gouges lies in the range 0.25–0.26 (Figures 3 and 5c). The slip-weakening distance is defined as the displacement at which $(\mu_p - \mu_{ss})$ reduces to 5% of $(\mu_p - \mu_{ss})$ (Figure 2) [*Mizoguchi et al.*, 2007]. The end-

Table 1. Summary of Experiments Run Until Steady State and Frictional Parameters Obtained

Experiment No.	wt % Calcite	wt % Clay	μ_i	μ_p	μ_{ss}	D_w	Total Displacement (m)	Experiment No.	wt % Calcite	wt % Clay	μ_i	μ_p	μ_{ss}	D_w	Total Displacement (m)
Calcite + Illite-Smectite								Calcite + Montmorillonite							
Dry Gouges															
394	100	0	0.53	0.75	0.25	0.58	7.05	394	100	0	0.53	0.75	0.25	0.58	7.05
455	80	20	0.54	0.72	0.33	0.29	0.92	424	80	20	0.51	0.75	0.33	0.36	0.62
452	50	50	0.56	0.76	0.23	0.44	1.92	420	50	50	0.55	0.69	0.31	0.19	0.54
405	0	100	0.54	0.63	0.25	0.17	0.73	395	0	100	0.58	0.61	0.26	0.2	1.04
Wet Gouges															
414	100	0	0.56	0.6	0.19	0.36	1.6	414	100	0	0.56	0.6	0.19	0.36	1.6
479	90	10	0.52	0.49	0.26	0.34	1.06	477	90	10	0.38	0.38	0.09	-	1.36
457	80	20	0.37	0.25	0.18	-	1.42	451	80	20	0.16	-	0.09	-	1.57
454	50	50	0.31	-	0.16	-	1.44	422	50	50	0.07	-	0.05	-	1.97
418	0	100	0.09	-	0.08	-	1.48	416	0	100	0.17	-	0.13	-	3.13

member calcite gouge displays a slip-weakening distance of 0.58 m, whereas the clay end-members become weaker over shorter distances of 0.17 m and 0.2 m for the illite-smectite and montmorillonite gouges, respectively (Figures 3 and 5d).

As would be expected, the curves for the gouges of mixed composition plot in positions intermediate between those of the end-members, although their overall trend is the same (Figure 3). Initial friction values again show little variation, ranging from 0.51 to 0.56 (Figure 5a), but μ_p decreases systematically as clay content increases, in both the calcite + illite-smectite and calcite + montmorillonite gouges (Figure 5b), as does D_w (Figure 5d).

3.1.2. Wet Gouges

The 100 wt % wet calcite gouge displays a slip-weakening curve similar to that of its dry equivalent (Figure 4), although values of μ_p, μ_{ss}, and D_w are slightly reduced (0.6, 0.19, and 0.36 m, respectively) (Figure 5). The other difference observed between the dry and wet calcite gouges is that whereas the dry gouge undergoes an immediate slip-hardening phase toward μ_p following the attainment of μ_i, the wet calcite gouge undergoes a brief slip-weakening phase, over a distance of just a few millimeters, before restrengthening and evolving toward μ_p (Figure 4).

Wet gouges containing 100% illite-smectite (Figure 4a) and 100% montmorillonite (Figure 4b), on the other hand, exhibit friction evolution curves that are markedly different to their dry equivalents. First, they display a significantly reduced μ_i of 0.09 for illite-smectite and 0.17 for montmorillonite (Figure 5a). Then, as for the wet calcite gouge, μ_i is followed by an immediate slip-weakening phase. The difference is that as slip proceeds, slip hardening does not occur at any stage in the wet clay gouges, and consequently, a peak in friction is never attained. Instead, friction evolves toward steady state values almost immediately at the onset of slip (Figure 4). Furthermore, the μ_{ss} values are very low: 0.08 for the illite-smectite end-member and 0.13 for the montmorillonite end-member (Figure 5c). Considering that these gouges are weak from the onset of slip, we do not assign them a slip-weakening distance.

The behavior of the mixtures of calcite + phyllosilicate is very much dependent on the phyllosilicate composition and content. In calcite + illite-smectite gouges (Figure 4a), there is a systematic decrease in frictional strength as the clay content is increased (Figures 5a–5c). At 10% clay, there is still a peak in friction, but its attainment is delayed; as in the wet calcite gouge, after the attainment of μ_i, the gouge undergoes slip weakening, followed by a brief restrengthening phase to a peak value of 0.49, before again undergoing slip weakening to steady state sliding. A similar friction evolution is observed at 20% illite-smectite, but the peak in friction is drastically reduced to just 0.25, which may be considered negligible. At 50 wt % illite-smectite, the peak in friction is eradicated altogether. Steady-state friction values also decrease with increasing clay content, falling from 0.26 at 10% illite-smectite, to 0.16 at 50%.

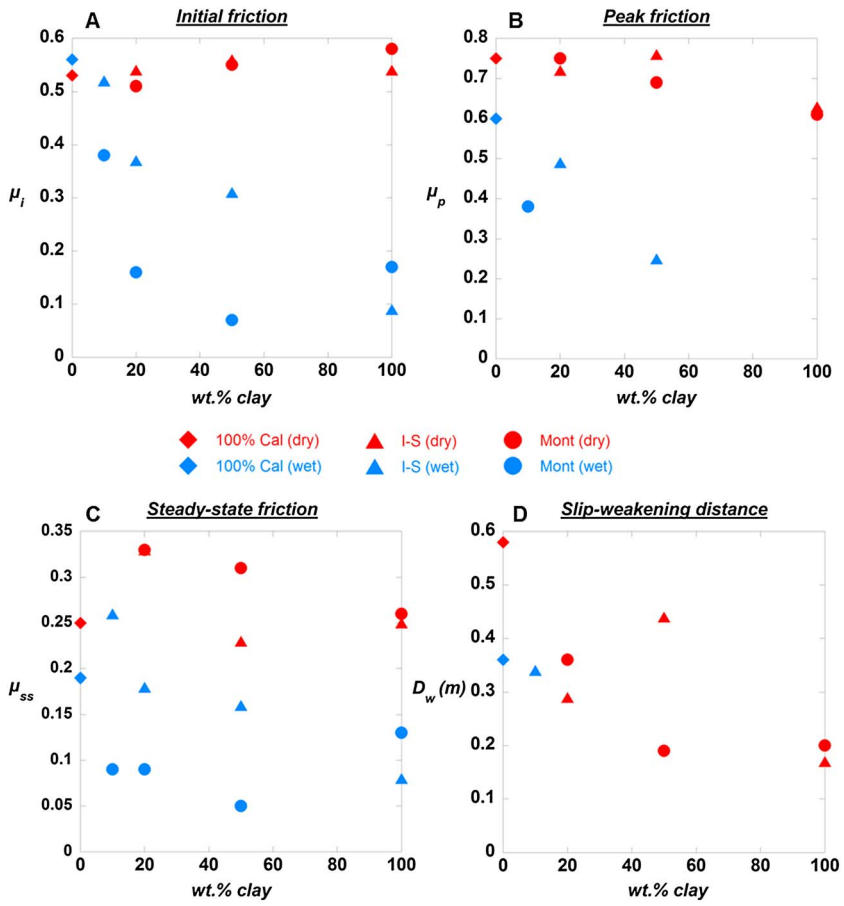

Figure 5. Summary plots showing evolution of frictional parameters as a function of increasing clay content. A key for all the plots is shown in the center of the figure. (a) Initial friction values are relatively constant for dry gouges but decrease with increasing clay content for wet gouges. (b) Peak friction values decrease slightly with increasing clay content for dry gouges, but this trend is much more enhanced for the wet gouges, to the extent that a peak in friction is absent for the most clay-rich gouges. (c) Steady state friction values show an overall decrease with increasing clay content for both dry and wet gouges. (d) D_w values again show an overall decreasing trend with increasing clay content, although in the case of wet clay-bearing gouges that do not exhibit a peak in friction, a slip-weakening distance is not applicable.

In the calcite + montmorillonite gouges under wet conditions (Figure 4b), μ_i values decrease as clay content increases (Figure 5a), but during subsequent slip, they display very similar strengths, regardless of clay content (Figure 5c). The exception is the 50 wt % montmorillonite gouge, which has a μ_i value of just 0.07, less than half that of the montmorillonite end-member, and it remains anomalously weak throughout the experiment. It should, however, be remembered that the 100% montmorillonite gouge was deformed under a lower normal load of 1.2 MPa, which could explain why it displays greater strength than the 50% montmorillonite gouge. Despite these subtle anomalies, all of the montmorillonite-bearing gouges exhibit the same frictional evolution during the experiments, in that none of them display a peak in friction, even when clay content is just 10 wt %. All of the mixtures evolve to steady state sliding, at values of μ_{ss} between 0.05 and 0.09, as soon as slip initiates. It should also be noted that for ≥20 wt % montmorillonite, the μ_i value is less than the yield strength of the gouge (Figures 4b and 6 of Text S4); this further illustrates just how weak these gouges are right from the onset of slip.

3.2. Microstructural Observations

Thin sections were analyzed using a field emission scanning electron microscope. Unsheared gouges were prepared by sectioning gouges that had been held under 9 MPa of normal load for 3 min, allowing examination of the initial microstructure of the gouge prior to shearing. Deformed gouges were prepared by sectioning the sheared gouges in an orientation normal to the shear plane and tangential to the direction of rotary shear. We refer to the entire width of the deformed gouge as the "slip zone" produced

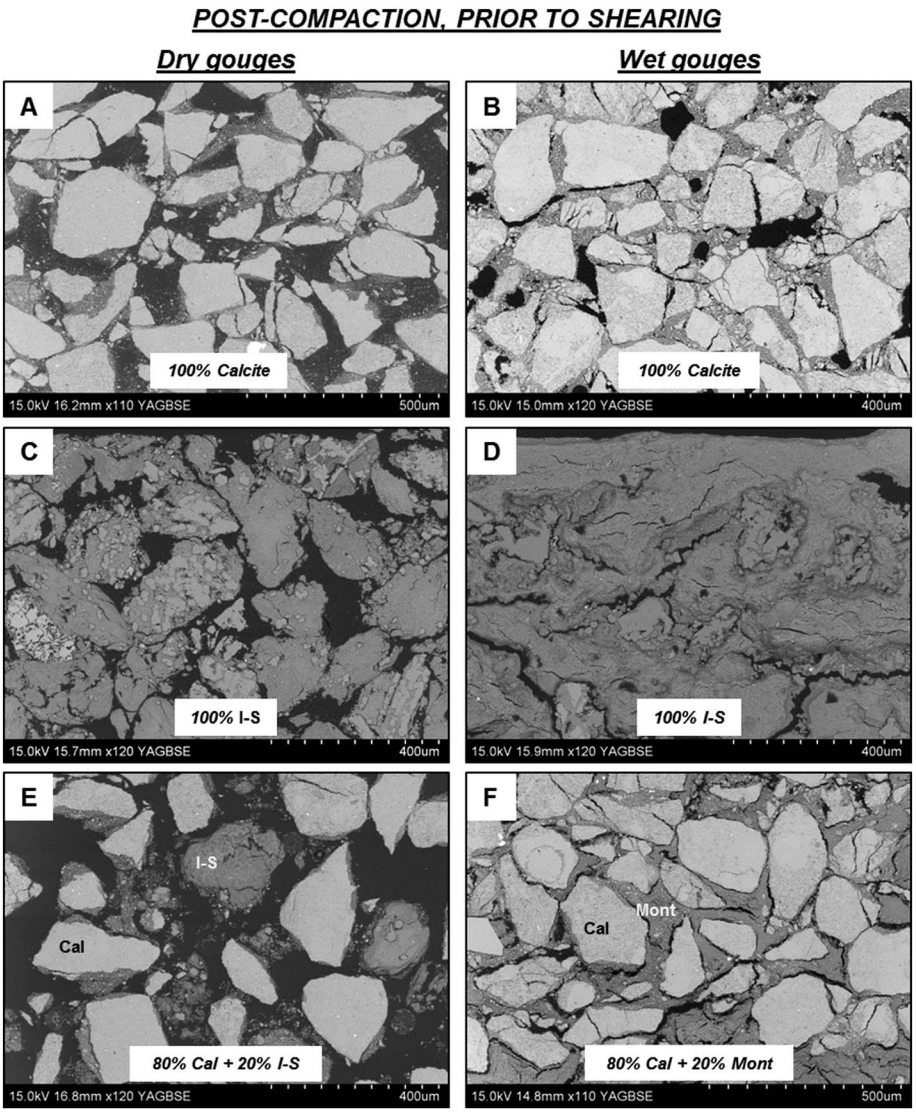

Figure 6. Initial microstructure of the gouges recovered after being held under 9 MPa normal load for 3 min, prior to shearing. See main text for full description. (a) 100% calcite, dry. (b) 100% calcite, wet. (c) 100% illite-smectite, dry. (d) 100% illite-smectite, wet. (e) 80% calcite + 20% illite-smectite, dry. (f) 80% calcite + 20% montmorillonite, wet.

during the experiment. Each slip zone contains a principal slip surface (PSS), where the majority of the rotary shear displacement is accommodated. The sample typically splits along the PSS on removal from the apparatus. In some experiments, slip appears to localize into a narrow zone adjacent to the PSS and this region is referred to as the principal slip zone (PSZ). Alongside the images presented in Figures 6–9, we present supporting images in Texts S5–S7.

3.2.1. Unsheared Gouges (Postcompaction)

The initial microstructure of the 100 wt % calcite gouge under dry conditions comprises discrete, angular grains of calcite (Figure 6a). The gouges were sieved to obtain an average starting grain size $< 250\ \mu m$. Many of the calcite grains are rimmed by a much finer powder of calcite grains averaging ~1 μm diameter (Figure 6a). These finer grains were likely produced during crushing and sieving of the gouges and adhered to the larger grains due to electrostatic charges and/or moisture on grain surfaces. The appearance of the 100 wt % calcite gouge under wet conditions is very similar to its dry equivalent, except that there is a greater amount of the fine calcite powder surrounding and in between the larger calcite grains (Figure 6b). This is likely due to the wet gouge being more cohesive and therefore the powder being more easily retained during thin-section preparation.

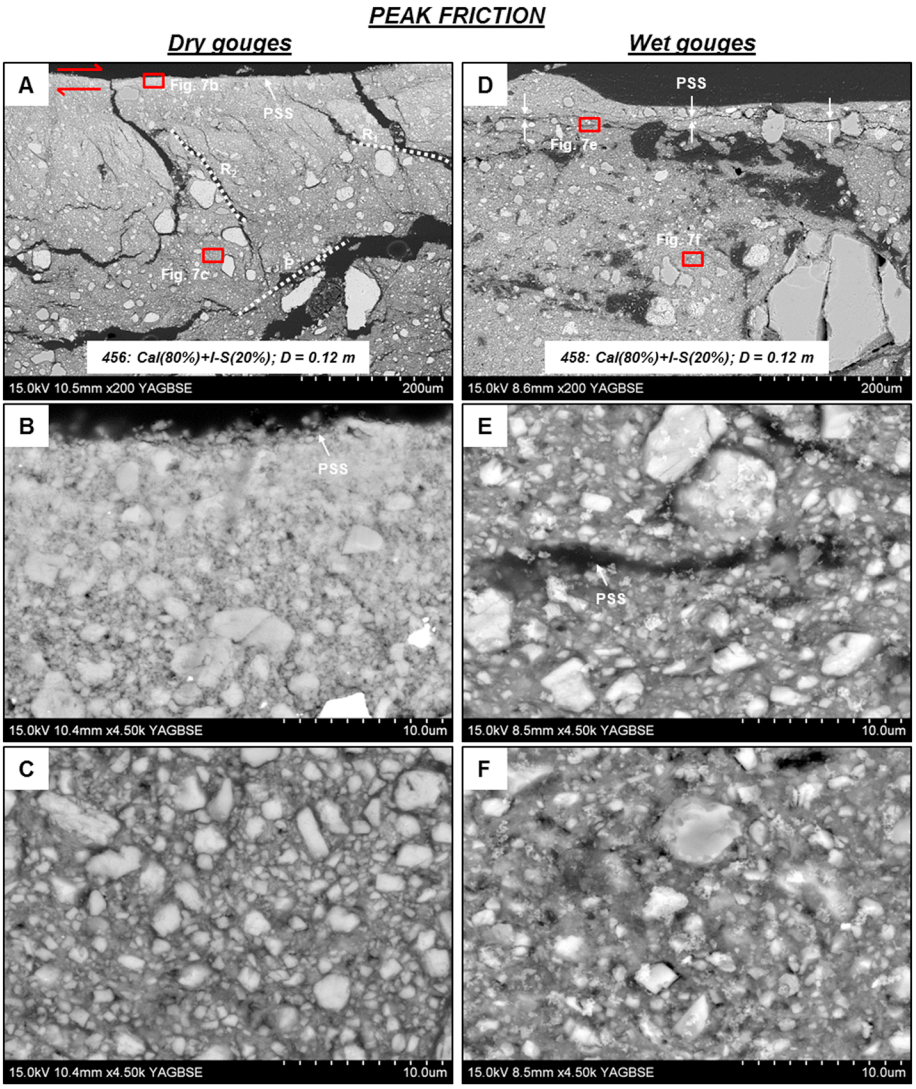

Figure 7. Deformed microstructures after recovery of gouges at peak friction. See main text for full description. (a) 80% calcite + 20% illite-smectite, dry. Overview of slip zone showing location of PSS. Examples of Riedel shear structures are labeled and the sense of shear inferred. R_2 shears dominate the fabric in the upper part of the slip zone, and *P* shears dominate the fabric in the central part of the slip zone in the lower portion of the image. (b) Zoomed in image of PSS and adjacent region in Figure 7a. (c) Zoomed in image of matrix within central slip zone of Figure 7a. (d) 80% calcite + 20% illite-smectite, wet. Overview of slip zone showing location of a very vague and undulating PSS. (e) Zoomed in image of PSS and adjacent region shown in Figure 7d. (f) Zoomed in image of matrix within central slip zone of Figure 7d.

The initial microstructure of the 100 wt % clay gouges under dry conditions comprises discrete agglomerates of clay particles, which have random shapes and orientations (Figure 6c); no fabric is developed. The initial microstructure of the 100 wt % clay gouges under wet conditions is rather different. Discrete agglomerates no longer exist; instead, when wet, the agglomerates appear to merge together upon compaction to form a mass of interconnected clay material, although still no fabric is formed (Figure 6d).

For the mixed calcite + phyllosilicate gouges, the initial microstructure when dry again comprises discrete grains of calcite and agglomerates of clay (Figure 6e). However, when wet, the clays once again merge together upon compaction and disperse throughout the gouge, forming a network of interconnected clay surrounding the calcite grains (Figure 6f).

3.2.2. Sheared Gouges: Peak Friction

The microstructure of dry gouges sheared until peak friction is characterized by the formation of a sharp, but sometimes wavy, PSS (Figures 7a and 7b; see also Figures 1–4 of Text S6). R_1 shears are already well

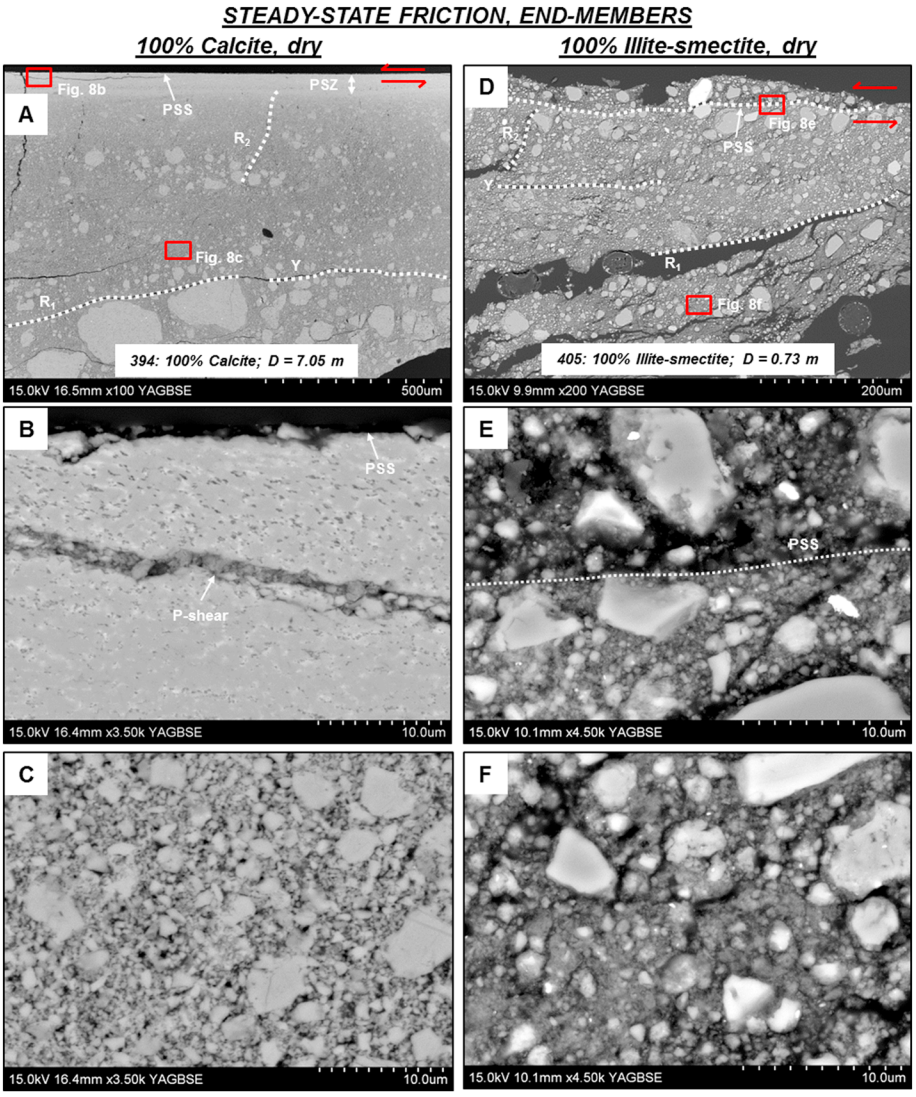

Figure 8. Deformed microstructures of dry end-member gouges after recovery during steady state sliding. See main text for full description. (a) 100% calcite, dry. Overview of slip zone showing location of PSS and PSZ. Examples of Riedel shear structures are labeled and the sense of shear inferred. R_1 shears dominate the fabric in the lower part of the slip zone, while higher-angle R_2 shears dominate the fabric in the upper part of the slip zone. (b) Zoomed in image of region adjacent to PSS and PSZ shown in Figure 8a. A *P* shear transects the center of the image. The dark spots scattered throughout the PSZ are holes, inferred to be the result of degassing as a consequence of thermal decomposition of calcite. (c) Zoomed in image of matrix within central slip zone of Figure 8a. (d) 100% illite-smectite, dry. Overview of slip zone showing location of PSS. Examples of Riedel shear structures are labeled and the sense of shear inferred. (e) Zoomed in image of PSS and adjacent region shown in Figure 8d. (f) Zoomed in image of matrix within central slip zone of Figure 8d.

developed within the slip zone at this stage, and R_2, *P*, and *Y* shears are present in some but not all cases (Figure 7a). Significant grain size reduction is evident throughout the gouge layers recovered at peak friction (Figures 7a–7c), when compared with the initial starting material (Figures 6a, 6c, and 6e). Grain size reduction is more intense in close proximity to the PSS (Figure 7b) than it is in the lower parts of the slip zone (Figure 7c), in some cases producing nanoparticle-sized material adjacent to the PSS (Figure 7b).

The wet gouges display quite a different microstructure when sheared until peak friction. There is no well-defined PSS in the wet gouges but instead just a poorly defined wavy surface, which likely corresponds to the PSS (Figures 7d and 7e). Unlike the dry gouges, there is no Riedel shear development within the slip zone. Significant grain size reduction has occurred, but it is not as intense as in the dry gouges. This is particularly evident when examining the region adjacent to the PSS (Figure 7e), where grain size appears

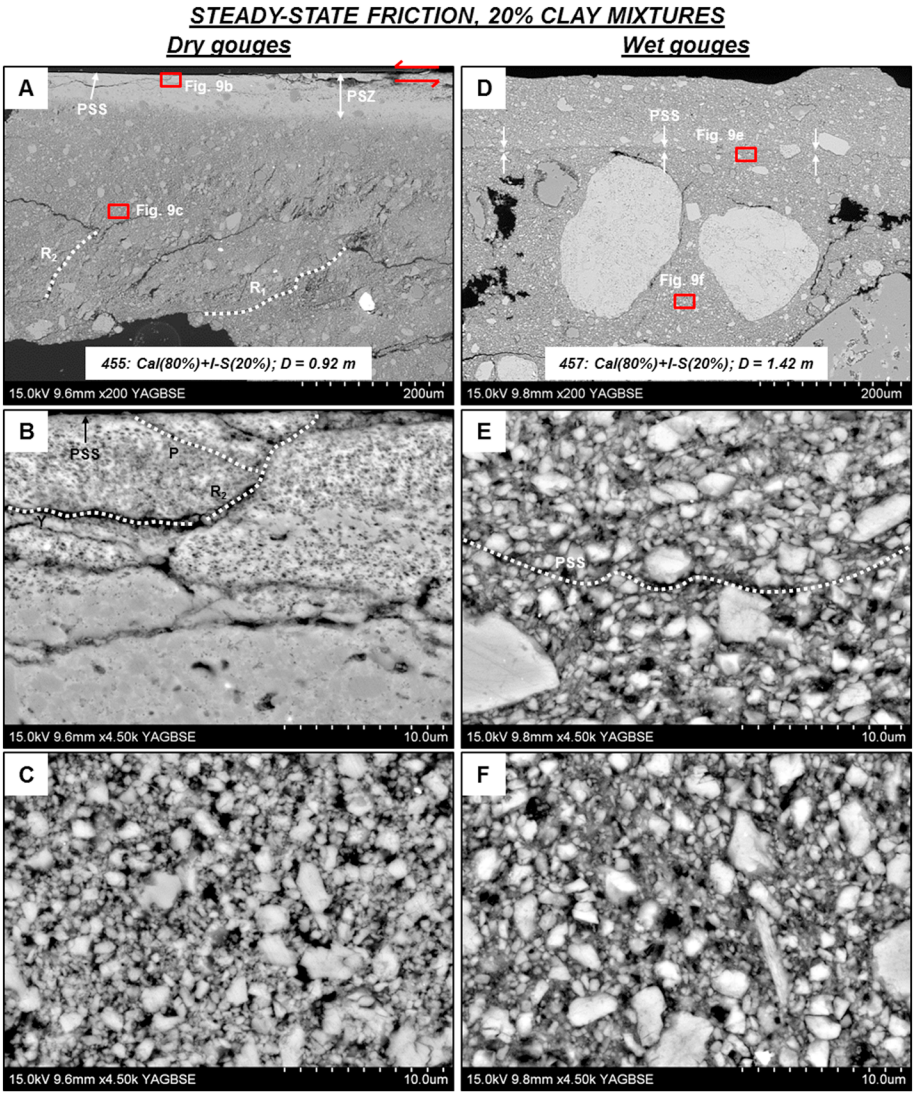

Figure 9. Deformed microstructures after recovery of gouges containing 20 wt % clay during steady state sliding. See main text for full description. (a) 80% calcite + 20% illite-smectite, dry. Overview of slip zone showing location of PSS and PSZ. Examples of Riedel shear structures are labeled and the sense of shear inferred. Fabric within the slip zone is dominated by R_1 shears. (b) Zoomed in image of PSZ shown in Figure 9a. R_1, *P*, and *Y* shears are present within the PSZ. The black spots scattered throughout the PSZ are holes, inferred to be degassing bubbles as a consequence of calcite decarbonation. (c) Zoomed in image of matrix within central slip zone of Figure 9a. (d) 80% calcite + 20% illite-smectite, wet. Overview of slip zone showing location of PSS. (e) Zoomed in image of PSS and adjacent region shown in Figure 9d. (f) Zoomed in image of matrix within central slip zone of Figure 9d.

very similar to that observed away from the PSS (Figure 7f). In addition, large grains up to 200 μm diameter, which appear to have undergone minimal deformation, remain in the slip zone (Figure 7d).

3.2.3. Sheared Gouges: Steady State

The microstructure of the dry gouges deformed until steady state friction varies slightly depending on gouge composition. In the 100% dry calcite gouge, the PSS (Figures 8a and 8b) is much sharper and straighter than it was at peak friction (see Figure 1 of Text S6). As at peak friction, there is a marked reduction in grain size toward the PSS. In addition, a PSZ, up to 60 μm wide, is formed adjacent to the PSS. The PSZ comprises highly compacted, ultrafine-grained calcite, which is scattered with bubbles (Figure 8b). The grain size in the bulk of the gouge, i.e., away from the PSZ, does not differ greatly to that observed at peak friction (compare Figures 8c and Figure 1c of Text S6). R_1 shears are extensive in the lower part of the slip zone

and are sometimes rotated into a *Y* orientation (Figure 8a). R_2 shears are also common, more so toward the upper part of the slip zone. Smaller-scale R_1, *Y*, and *P* shears are also common within the PSZ (Figure 8b).

In the 100% dry clay gouges (Figures 8d–8f and Figure 1 of Text S7), the PSSs are not as sharp and straight as in the 100% calcite sample (Figures 8a and 8b). It should be noted that the 100% illite-smectite and 100% montmorillonite gouges have experienced smaller displacements (0.73 m and 1.04 m total displacement, respectively) than the 100% calcite gouge (7.05 m total displacement). However, we see that in other calcite-rich gouges deformed to similar displacements as the clay end-members, the PSSs are still very sharp and straight compared to those in the clay gouges (e.g., Figures 9a, 9b, 10a, and 10b, plus Figures 2 and 3 of Text S7). Thus, it appears that a wispy, undulating PSS is a feature unique to the 100% clay gouges, regardless of displacement. In addition, grain size reduction adjacent to the PSS (Figure 8e) is not as intense in the clay end-member gouges as in the 100% calcite gouge; grain size is more uniform over the whole slip zone (compare Figures 8e and 8f), and subsequently, no PSZ is present. However, there are Riedel shears developed throughout the slip zone (Figure 8d).

In the dry gouges of mixed composition (Figures 9a–9c and 10a–10c), the microstructure at steady state is somewhat intermediate between those of the end-members described above. In the presence of 20 wt % clay, microstructures are comparable to those in the calcite end-member. PSSs are very sharp and straight, and intense grain size reduction has occurred toward these surfaces (Figures 9a and 9b; see also Figure 2 of Text S7). In the 20 wt % illite-smectite gouge, there is a very well developed, continuous PSZ up to 65 μm wide (Figures 9a and 9b), whereas in the 20 wt % montmorillonite gouge, the PSZ is highly variable in width, being only a few microns in some places but up to 35 μm in others (Figure 2 of Text S7). Despite differences in development, the PSZs in the illite-smectite- and montmorillonite-bearing gouges are of similar nature: they comprise a matrix of highly compacted, ultrafine-grained calcite + clay, and both contain bubbles, replicating the PSZ microstructure observed in the 100% calcite gouge (Figure 9b and Figure 2b of Text S7). As in the 100% calcite gouge, the slip zone has a fabric characterized by R_1, R_2, and *Y* shears (Figure 9a and Figure 2a of Text S7), and the grain size out width of the PSZ does not vary greatly from peak friction to steady state (compare Figures 7c and 9c).

In the presence of 50 wt % clay, the microstructures are different for the illite-smectite-bearing and the montmorillonite-bearing gouge. The 50 wt % illite-smectite gouge has a microstructure unlike any of the other gouges in that there is quite a distinct partitioning of strain across the slip zone, with different domains separated by *Y* shears (Figure 3a of Text S7). Despite this, it still has a sharp PSS as in all the other dry gouges, but it is relatively rough in comparison (Figure 3b of Text S7). Increased grain size reduction is also observed in areas adjacent to the PSS (Figure 3b of Text S7). There is not a well-developed PSZ, but the compacted, ultrafine-grained material associated with PSZs in the 20 wt % clay samples is present in localized patches along the PSS (Figure 3b of Text S7). Where this compacted ultrafine-grained material is not present, the material adjacent to the PSS is characterized by predominantly submicron sized, subangular to subrounded clasts of calcite and flakes of phyllosilicate (Figure 3b of Text S7).

The 50 wt % montmorillonite gouge is similar to the 20 wt % montmorillonite gouge, in that it has a sharp, smooth PSS and a variably developed PSZ (up to 30 μm wide) (Figures 10a and 10b). Plus it has a pervasive fabric dominated by R_1 shears (plus some R_2 and *P* shears present within the PSZ) (Figures 10a and 10b). Once again, the PSZ (Figure 10b) is characterized by a matrix of compacted, ultrafine-grained calcite + clay and, in places, contains bubbles, although the bubbles are not as ubiquitous as in the gouges containing just 20 wt % clay (Figure 9b).

We were not able to recover any wet clay end-member gouges for thin sectioning; the swelling nature of the clays causes them to be easily extruded from the sample assembly during the experiments. Thus, we only describe here the observations made for gouges of mixed calcite + phyllosilicate composition. The wet clay-bearing gouges recovered after steady state sliding have a more fully developed, throughgoing PSS (Figures 9d and 10d; see also Figures 4 and 5 of Text S7) than those recovered at peak friction (Figure 7d). However, the PSS is still quite a vague and undulating feature (Figures 9e and 10e) and not as sharp and straight as in the dry gouges (Figures 9b and 10b). The PSS does not appear to be defined by anything in particular; e.g., we do not observe any alignment of phyllosilicates along the PSS. Several large, subrounded grains, up to 230 μm in diameter, remain within the central portion of the slip zone (Figures 9d and 10d). This is more than twice the size of the largest grains in the central slip zone of their

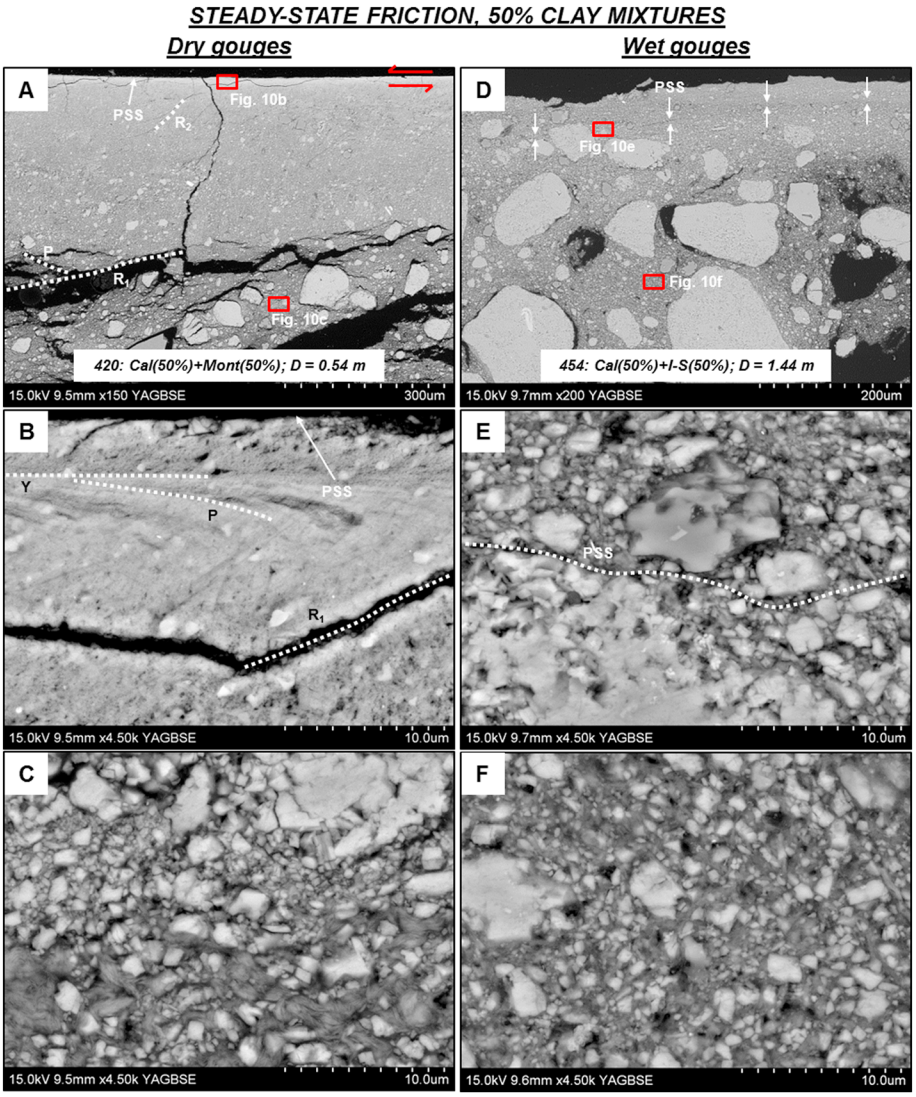

Figure 10. Deformed microstructures after recovery of gouges containing 50 wt % clay during steady state sliding. See main text for full description. (a) 50% calcite + 50% montmorillonite, dry. Overview of slip zone showing location of PSS. Examples of Riedel shear structures are labeled and the sense of shear inferred. R_1 shears dominate the fabric within the slip zone. A PSZ up to 30 μm wide is formed adjacent to the PSS (see Figure 10b) but is unresolvable at the scale of the image. (b) Zoomed in image of PSS and PSZ shown in Figure 10a. The 5 μm wide zone right at the top of the image, delimited from the rest of the PSZ by a subhorizontal *Y* shear, contains rounded to elongate black spots, which we interpret to be degassing bubbles as a result of calcite decarbonation. Several very fine *P* shears are visible just beneath this zone as well as the intersecting *P* and R_1 shears in the lower part of the image. (c) Zoomed in image of matrix within central slip zone of Figure 10a. (d) 50% calcite + 50% illite-smectite, wet. Overview of slip zone showing location of PSS, which is very vague and almost unresolvable at the scale of the image. (e) Zoomed in image of PSS and adjacent region in Figure 10d. (f) Zoomed in image of matrix within central slip zone of Figure 10d.

dry equivalents, which are also more subangular in nature (Figures 9a and 10a). In addition, no PSZ is developed; the matrix grain size adjacent to the PSS (Figures 9d and 10d) is comparable to that in the lower parts of the slip zone (Figures 9f and 10f) and is certainly much coarser than in the dry gouge equivalents (Figures 9b and 10b). Finally, none of the PSZ characteristics observed in the dry gouges sheared until steady state, i.e., the presence of highly compacted ultrafine-grained material or bubbles, are observed in the wet gouges. Fabric development in the slip zone, in the form of Riedel shears, is also absent. These microstructures are consistent for all wet clay-bearing gouges, the only difference being that in the gouges containing just 10 wt % clay (Figures 4 and 5 of Text S7), the large grains in the central portion of the slip zone are more angular than in the gouges that have higher clay contents.

4. Discussion

4.1. Frictional Evolution of Dry Versus Wet Clay-Bearing Gouges

Our experimental results show a dramatic contrast in frictional behavior between dry and wet clay-bearing carbonate gouges. The dry clay-bearing gouges display typical high-velocity friction evolution curves that have been produced in numerous experiments on a wide range of materials [*Di Toro et al*., 2011]. The wet clay-bearing gouges, on the other hand, do not conform to a typical high-velocity frictional evolution, in that they undergo little or no slip hardening after the attainment of the initial friction value and thus do not attain a peak in friction during the experiments. This behavior replicates that observed during previous high-velocity friction experiments on saturated clay-bearing gouges [*Ferri et al*., 2010; *Ujiie and Tsutsumi*, 2010; *Faulkner et al*., 2011; *Ferri et al*., 2011; *Ujiie et al*., 2011, 2013]. However, these previous studies used natural gouges, in most cases with >50% clay. What we are able to show here by systematically varying the clay content in synthetic gouges is that just 10 wt % clay (in the case of montmorillonite) or 20 wt % clay (in the case of mixed-layer illite-smectite) is required to produce the same weakening behavior that is observed in clay-dominated gouges.

4.2. Microstructural Evolution of Dry Versus Wet Clay-Bearing Gouges

The contrasting frictional behaviors of the dry versus wet clay-bearing gouges are accompanied by starkly contrasting microstructures. The dry clay-bearing gouges are characterized by localized slip, which is accommodated along a very sharp, smooth PSS and within a variably developed PSZ. The PSS and PSZ have undergone intense cataclasis and wear and show evidence for frictional heating in excess of ~700°C, in the form of degassing bubbles within PSZs, which we infer to be a result of calcite decarbonation. The wet clay-bearing gouges, on the other hand, are characterized by a much more distributed style of deformation, whereby they lack a sharp PSS and a PSZ, and cataclasis appears to have been less intense. Additionally, none of the wet clay-bearing gouges show any evidence for calcite decarbonation, suggesting significantly lower amounts of frictional heating than in their dry equivalents. The observation of contrasting microstructures between dry and wet clay-bearing gouges sheared at seismic velocity is consistent with observations made in previous studies [e.g., *Ferri et al*., 2011; *Ujiie et al*., 2011; *French et al*., 2014]. A direct comparison would not be appropriate, due to the fact that these previous studies were conducted at much lower normal load (~1 MPa) than in our experiments, but it seems that wet clay-bearing gouges typically experience a less intense grain size reduction and shear fabric or foliation development than their dry counterparts.

The contrasting microstructures observed in the dry versus wet clay-bearing gouges suggest that it may be possible to explain their contrasting frictional behaviors through micromechanical processes. We propose a micromechanical model as follows. In the dry clay-bearing gouges, the initial microstructure comprises discrete clasts of calcite and agglomerates of clay (Figure 11a, panel 1). When slip initiates in these gouges, it is necessary for pervasive cataclasis to occur before slip can localize along a throughgoing PSS (Figure 11a, panel 2). Once the PSS has formed, then a large amount of wear must also occur in order to produce the smooth surfaces observed in the microstructures (Figures 9b and 10b). These processes explain the slip-hardening phase at the start of the dry experiments [e.g., *Biegel et al*., 1992, and references therein]. Once a PSS is well established, then slip localizes here and a PSZ forms adjacent to it (Figure 11a, panel 3). Because strain is concentrated along the PSS and within the PSZ, grain size in the remainder of the slip zone does not change significantly from peak friction to steady state sliding. The localization of slip results in intense frictional heating along the PSS and within the PSZ, enough to trigger calcite decarbonation (and perhaps implying that clay dehydration has also taken place, although microstructural evidence of this is not obvious). Mechanical wear and thermal decomposition processes also result in the production of nanoparticles within the PSZ and coating the PSS. A combination of thermal pressurization, dynamic recrystallization, and nanoparticle lubrication are likely responsible for the dynamic weakening behavior of the dry gouges, as invoked by previous studies [*Han et al*., 2007; *De Paola et al*., 2011a, 2011b; *Han et al*., 2011; *Smith et al*., 2013; *De Paola et al*., 2014].

In the wet clay-bearing gouges, on the other hand, the initial microstructure comprises an interconnected matrix of wet clay surrounding calcite grains (Figure 11b, panel 1). Saturated clays have been shown to be inherently weak, even at low slip velocities. The average coefficient of friction reported in the literature for wet montmorillonite is 0.18 [*Saffer et al*., 2001; *Saffer and Marone*, 2003; *Ikari et al*., 2007; *Moore and Lockner*, 2007;

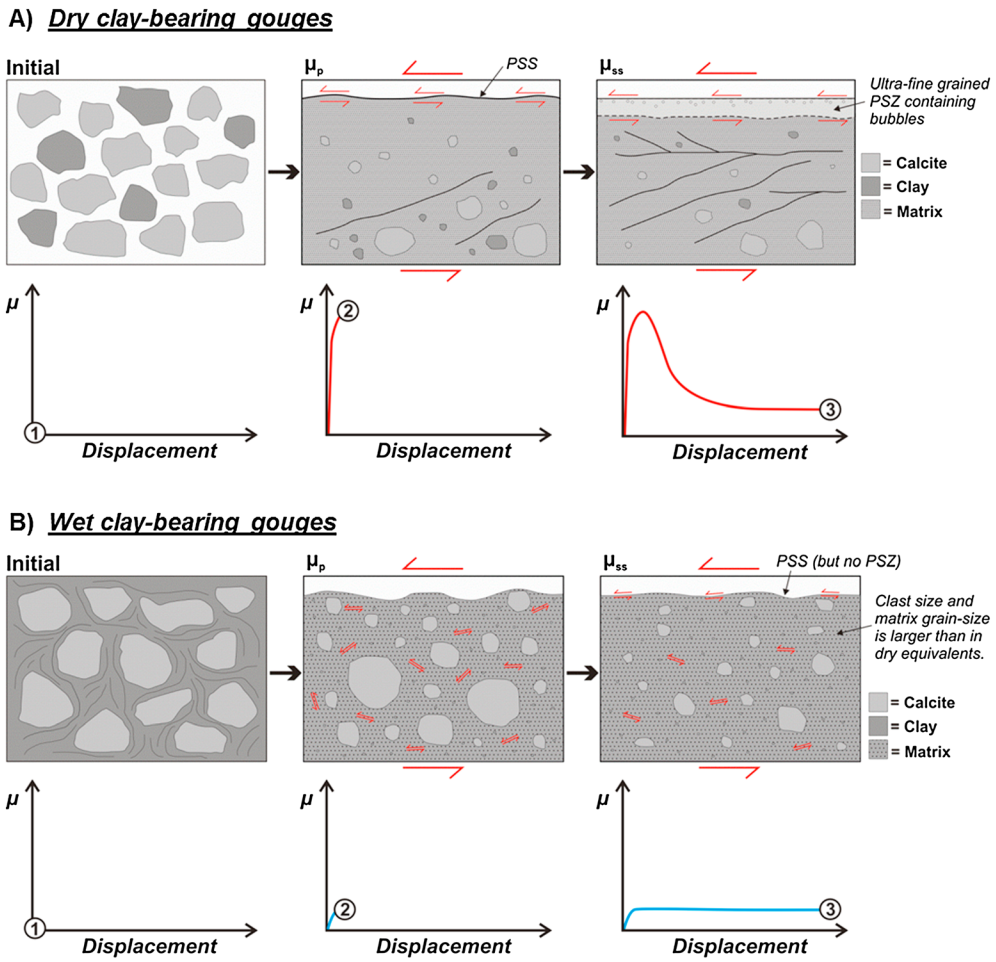

Figure 11. Proposed micromechanical model, based on microstructural observations, to explain the contrasting mechanical behavior, also depicted, of (a) dry clay-bearing gouges and (b) wet clay-bearing gouges. Panels show microstructural evolution from the initial starting material through to peak friction and steady state sliding. See main text for explanation.

Tembe et al., 2010; *Behnsen and Faulkner*, 2012] and for wet illite is 0.37 [*Morrow et al.*, 1992; *Saffer and Marone*, 2003; *Ikari et al.*, 2009; *Tembe et al.*, 2010; *Behnsen and Faulkner*, 2012]. Thus, when slip initiates, it preferentially occurs on the preexisting, weak clay lamellae, which are distributed throughout the gouge (Figure 11b, panel 2). This reduces the need for pervasive cataclasis to occur before slip is able to localize and explains the lack of slip hardening in the wet clay-bearing gouges. This theory is supported by the distributed style of deformation observed in the wet gouges, including the absence of a PSZ (Figure 11b, panel 3), plus the larger grain sizes in the deformed wet clay-bearing gouges in comparison to their dry equivalents. The fact that slip is not localized within a narrow zone, plus the low values of friction, would result in a far lesser amount of frictional heating in the wet gouges than in the dry ones. This would explain why there is no microstructural evidence for thermal decomposition of calcite having occurred in the wet clay-bearing gouges.

A PSS still forms in the wet gouges, and so it is evident that slip does attempt to localize. However, the mechanical processes involved during slip localization are different. In the dry clay-bearing gouges, slip localization is driven by cataclasis and wear, whereas in the wet clay-bearing gouges, it is likely driven by sliding on weak, water-saturated clay lamellae [*Moore and Lockner*, 2004, 2007]. This is reflected in the nature of the PSSs in the wet gouges, which are rather undulating (Figures 9e and 10e), suggesting that they are located where weak clay horizons are most readily available, as opposed to on a sharp slip plane where asperities have been broken and worn down by shearing. Given that we do not observe a throughgoing layer of aligned phyllosilicates along the PSS for slip to occur on, we would not rule out the

possibility that slip may actually occur on a thin film of water, which has been expelled from the gouge and become trapped along the PSS, as suggested by *Ferri et al*. [2010]. Alternatively, it may be that a throughgoing layer of aligned phyllosilicates is formed along the PSS, but it is so localized and narrow that it cannot be resolved with the scanning electron microscope. Or such a layer may be obscured by the sinking of calcite clasts into the layer as the sample relaxes postdeformation.

The slight difference in behavior between the wet illite-smectite bearing gouges and the wet montmorillonite-bearing gouges can be explained through the expansive capabilities of smectite clays. Upon saturation, smectite group clays allow water into their interlayer structure. It has been suggested that the extreme weakness of smectites may be due to sliding occurring on thin lubricating films of water located between clay interlayers [e.g., *Moore and Lockner*, 2004]. If this is the case, then it is not surprising that the mixed-layer illite-smectite clay should be stronger, because the illite component of the clay does not have the same expansive capability. Thus, the delayed peak in friction in experiments 479 and 457, containing 10 wt % and 20 wt % of illite-smectite, respectively, may be due to water-saturated smectite horizons within the gouge being consumed through comminution, before slip has fully localized. Thus, in order for slip to localize and proceed, some cataclasis is still necessary, hence the delayed slip-hardening phase.

As well as the saturated clays being inherently weak, the impermeable nature of the starting material created by the interconnected clay network (Figures 6d and 6f) would enhance pore fluid pressurization generated by shear-induced compaction, which would further reduce the strength of the gouge [e.g., *Blanpied et al*., 1992]. Gouge dilatancy triggered by pore fluid pressurization may also inhibit the localization of shear [e.g. *Rice et al*., 2014], consistent with our observation of a distributed style of deformation in the wet clay-bearing gouges. The initial weakening phase observed during experiments 457 and 479, and also during experiment 414 on the water-saturated 100% calcite gouge (Figure 4a), before they undergo slip hardening to attain their peak friction, is most likely due to a sudden pore fluid overpressure generated at the onset of slip.

4.3. Implications

4.3.1. Rupture Propagation in Clay-Bearing Carbonate Faults

Our results show that the presence of clay in fault gouge alone does not significantly affect the frictional behavior of a fault during earthquake propagation. However, if water is present within gouges containing as little as 10–20% clay, then they can become very weak and resistance to earthquake propagation is significantly reduced. As highlighted by *Faulkner et al*. [2011], the negligible fracture energy associated with saturated clay-bearing gouges means that very little energy is required to maintain rupture propagation, and so it would be energetically more feasible for a rupture to propagate all the way to the surface. Thus, while wide, phyllosilicate-rich zones in the shallow portions of faults may promote stable fault slip due to their velocity-strengthening properties [e.g., *Hsu et al*., 2006; *Holdsworth et al*., 2011], if these phyllosilicates become concentrated within narrow PSZs, they will likely facilitate earthquake propagation. The results have significant implications for seismic hazard assessment, particularly in the Northern Apennines of Italy, which has experienced a number of large earthquakes in recent years [e.g., *D'Agostino et al*., 2009]. This is an area where clays are sometimes present within the PSZs of earthquake-hosting carbonate faults (e.g., Figure 1) [*Collettini et al*., 2013; *Tesei et al*., 2013; *Bullock et al*., 2014; *Collettini et al*., 2014]. These natural gouges often display a foliated fabric as a result of previous slip events and/or aseismic creep during the interseismic period (e.g., Figure 9 of *Bullock et al*. [2014] and Figures 1–3 of Text S1). Rock/gouge samples with a preexisting fabric have been shown experimentally to have significantly lower strength than powdered gouge samples with no fabric [e.g., *Collettini et al*., 2009; *Niemeijer et al*., 2010]. It is therefore plausible that natural clay-bearing fault gouges could be even weaker than the results we have presented here for experiments on powdered gouges with no preexisting fabric. In addition, seismological models have invoked fluids as playing an important role in active seismicity in the Northern Apennines [e.g., *Miller et al*., 2004; *Di Luccio et al*., 2010; *Malagnini et al*., 2012]. The presence of fluids is supported by geological observations documenting pervasive calcite mineralization within and adjacent to PSZs, in the form of both veins (e.g., Figures 1c and 1e) and hydraulic breccias [*Tesei et al*., 2013; *Bullock et al*., 2014; *Collettini et al*., 2014]. The clays within the PSZs likely act as seals and promote the generation of high fluid pressures along faults [*Blanpied et al*., 1992].

The evident interaction of fluids with clay-bearing carbonate fault gouges may be a contributing factor toward the common occurrence of surface-breaking scarps in the Northern Apennines [e.g., *Vittori et al*., 2000; *Guerrieri et al*., 2009].

So far, such results concerning the extreme weakness of saturated clay gouges at seismic slip velocities have been considered with relation to subduction zone earthquakes [*Ujiie and Tsutsumi*, 2010; *Faulkner et al*., 2011; *Ujiie et al*., 2013], which appear to propagate through the clay-rich sediments of accretionary wedges with relative ease [e.g., *Ide et al*., 2011]. However, clays are a common feature of many upper crustal earthquake-hosting faults [e.g., *Wu et al*., 1975; *Vrolijk and van der Pluijm*, 1999; *Holdsworth*, 2004], where fluids are often invoked to play a major role during faulting [e.g., *Sibson*, 1981]. Thus, these results are relevant for assessing the behavior and potential capability of any clay-bearing seismogenic fault, regardless of its tectonic setting.

4.3.2. Seismic Markers in Clay-Bearing Carbonate Faults

In recent years, it has become increasingly common for structural geologists to try and distinguish indicators of seismic versus aseismic slip, both from laboratory and field observations. A growing range of so-called "coseismic slip indicators" have been documented, for example, pseudotachylytes [*Sibson*, 1975], dynamically recrystallized calcite [*Smith et al*., 2013; *De Paola et al*., 2014], fault mirrors [*Fondriest et al*., 2013; *Siman-Tov et al*., 2013], clay mineral transformations [*Yamaguchi et al*., 2011; *Bullock et al*., 2014], biomarkers [*Savage et al*., 2014], degassing bubbles, and "quenched" calcite crystals [*Collettini et al*., 2013; *Bullock et al*., 2014]. All of these coseismic signatures are associated with localized slip and frictional heating. In contrast, fault gouges exhibiting distributed deformation, particularly those rich in velocity-strengthening phyllosilicates, are generally interpreted as representing aseismic portions of faults [e.g., *Faulkner et al*., 2003; *Holdsworth et al*., 2011]. The fault gouges such as those produced during our high-velocity experiments on water-saturated clay-bearing gouges do not contain any seismic markers and exhibit distributed deformation. Thus, they may be overlooked as seismogenic faults if observed in nature, when, in fact, they have the potential to allow capable faulting and the production of devastating surface ruptures. In addition, the fact that phyllosilicates are prone to creep makes it likely that even seismic markers such as those produced during our dry run experiments, e.g., localized PSZs containing signatures of thermal decomposition, would be overprinted during the interseismic period. Therefore, clay-bearing carbonate gouges should be approached with a high degree of caution when considering the seismic history and potential of a natural fault zone.

5. Conclusions

High-velocity friction experiments performed on mixtures of calcite + illite-smectite and calcite + montmorillonite produce very different results depending on whether the gouges are deformed under room humidity (dry) or water-saturated (wet) conditions. Dry clay-bearing gouges display a friction evolution curve that is typical of those associated with high-velocity friction experiments on a wide range of rock types. The wet clay-bearing gouges, on the other hand, do not exhibit a typical frictional evolution, in that they undergo little or no slip hardening, and therefore do not attain a peak in friction. Instead, they attain steady state frictional sliding almost immediately at the onset of slip, at values of $\mu_{ss} \ll 0.2$. This behavior is observed even when the clay content is just 10 wt %, in the case of montmorillonite, and 20 wt %, in the case of illite-smectite. These results have significant implications for seismic hazard assessment, as they show that calcite gouges containing small amounts of wet clay will potentially present very little resistance to seismic rupture propagation, enhancing the potential for surface-rupturing capable faulting in a variety of tectonic settings.

In our experiments we attribute the observed weak behavior of the wet clay-bearing gouges to their initial microstructure prior to shearing, which consists of an interconnected network of wet clay surrounding the calcite grains. Thus, as slip initiates, it preferentially occurs on the clay horizons distributed throughout the gouge, which are inherently weak. In the dry gouges, cataclasis must occur before slip can localize and trigger dynamic weakening, and thus, they present a much greater resistance to frictional sliding. The lack of slip localization and the low friction values in the wet clay-bearing gouges significantly reduce the amount of frictional heating generated. This means that natural seismogenic fault gouges containing small amounts of wet clay will not necessarily exhibit the signatures that are so commonly thought to be associated with seismic slip.

Acknowledgments
Brett Carpenter and Cristiano Collettini are thanked for their constructive reviews which helped to clarify and strengthen the manuscript. This work was funded by the Natural Environment Research Council through a NERC PhD studentship NE/J500215/1 awarded to R.J.B. and a NERC standard grant NE/H021744/1 awarded to N.D.P. The raw data presented in this paper are available upon request from the corresponding author.

References

Barchi, M., G. Minelli, and G. Pialli (1998), The CROP 03 profile: A synthesis of results on deep structures of the Northern Apennines, *Mem. Soc. Geol. Ital.*, *52*, 383–400.

Behnsen, J., and D. R. Faulkner (2012), The effect of mineralogy and effective normal stress on frictional strength of sheet silicates, *J. Struct. Geol.*, *42*, 49–61.

Biegel, R. L., W. Wang, C. H. Scholz, G. N. Boitnott, and N. Yoshioka (1992), Micromechanics of rock friction: 1. Effects of surface roughness on initial friction and slip hardening in westerly granite, *J. Geophys. Res.*, *97*(B6), 8951–8964, doi:10.1029/92JB00042.

Blanpied, M. L., D. A. Lockner, and J. D. Byerlee (1992), An earthquake mechanism based on rapid sealing of faults, *Nature*, *358*(6387), 574–576.

Boutareaud, S., D.-G. Calugaru, R. Han, O. Fabbri, K. Mizoguchi, A. Tsutsumi, and T. Shimamoto (2008), Clay-clast aggregates: A new textural evidence for seismic fault sliding?, *Geophys. Res. Lett.*, *35*, L05302, doi:10.1029/2007GL032554.

Brantut, N., A. Schubnel, J. N. Rouzaud, F. Brunet, and T. Shimamoto (2008), High-velocity frictional properties of a clay-bearing fault gouge and implications for earthquake mechanics, *J. Geophys. Res.*, *113*, B10401, doi:10.1029/2007JB005551.

Bullock, R. J., N. De Paola, R. E. Holdsworth, and J. Trabucho-Alexandre (2014), Lithological controls on the deformation mechanisms operating within carbonate-hosted faults during the seismic cycle, *J. Struct. Geol.*, *58*, 22–42, doi:10.1016/j.jsg.2013.10.008.

Carpenter, B., C. Marone, and D. Saffer (2011), Weakness of the San Andreas Fault revealed by samples from the active fault zone, *Nat. Geosci.*, *4*(4), 251–254.

Chester, F. M., et al. (2013), Structure and composition of the plate-boundary slip zone for the 2011 Tohoku-Oki earthquake, *Science*, *342*(6163), 1208–1211, doi:10.1126/science.1243719.

Chiaraluce, L. (2012), Unravelling the complexity of Apenninic extensional fault systems: A review of the 2009 L'Aquila earthquake (Central Apennines, Italy), *J. Struct. Geol.*, *42*, 2–18, doi:10.1016/j.jsg.2012.06.007.

Collettini, C., N. De Paola, R. Holdsworth, and M. Barchi (2006), The development and behaviour of low-angle normal faults during Cenozoic asymmetric extension in the Northern Apennines, Italy, *J. Struct. Geol.*, *28*(2), 333–352.

Collettini, C., A. Niemeijer, C. Viti, and C. Marone (2009), Fault zone fabric and fault weakness, *Nature*, *462*(7275), 907–910. [Available at http://www.nature.com/nature/journal/v462/n7275/suppinfo/nature08585_S1.html.]

Collettini, C., A. Niemeijer, C. Viti, S. A. F. Smith, and C. Marone (2011), Fault structure, frictional properties and mixed-mode fault slip behavior, *Earth Planet. Sci. Lett.*, *311*(3), 316–327.

Collettini, C., C. Viti, T. Tesei, and S. Mollo (2013), Thermal decomposition along natural carbonate faults during earthquakes, *Geology*, *41*(8), 927–930, doi:10.1130/g34421.1.

Collettini, C., B. M. Carpenter, C. Viti, F. Cruciani, S. Mollo, T. Tesei, F. Trippetta, L. Valoroso, and L. Chiaraluce (2014), Fault structure and slip localization in carbonate-bearing normal faults: An example from the Northern Apennines of Italy, *J. Struct. Geol.*, *67*, 154–166, doi:10.1016/j.jsg.2014.07.017.

D'Agostino, N., S. Mantenuto, E. D'Anastasio, A. Avallone, M. Barchi, C. Collettini, F. Radicioni, A. Stoppini, and G. Fastellini (2009), Contemporary crustal extension in the Umbria–Marche Apennines from regional CGPS networks and comparison between geodetic and seismic deformation, *Tectonophysics*, *476*(1–2), 3–12, doi:10.1016/j.tecto.2008.09.033.

De Paola, N., G. Chiodini, T. Hirose, C. Cardellini, S. Caliro, and T. Shimamoto (2011a), The geochemical signature caused by earthquake propagation in carbonate-hosted faults, *Earth Planet. Sci. Lett.*, *310*(3), 225–232.

De Paola, N., T. Hirose, T. Mitchell, G. Di Toro, C. Viti, and T. Shimamoto (2011b), Fault lubrication and earthquake propagation in thermally unstable rocks, *Geology*, *39*(1), 35–38.

De Paola, N., R. E. Holdsworth, C. Viti, C. Collettini, I. Faoro, and R. J. Bullock (2014), Can grain size sensitive creep lubricate faults during earthquake propagation?, paper presented at AGU Fall meeting, San Francisco, Calif.

Di Luccio, F., G. Ventura, R. Di Giovambattista, A. Piscini, and F. Cinti (2010), Normal faults and thrusts reactivated by deep fluids: The 6 April 2009 M_w 6.3 L'Aquila earthquake, central Italy, *J. Geophys. Res.*, *115*, B06315, doi:10.1029/2009JB007190.

Di Toro, G., R. Han, T. Hirose, N. De Paola, S. Nielsen, K. Mizoguchi, F. Ferri, M. Cocco, and T. Shimamoto (2011), Fault lubrication during earthquakes, *Nature*, *471*(7339), 494–498.

Faulkner, D. R., T. M. Mitchell, J. Behnsen, T. Hirose, and T. Shimamoto (2011), Stuck in the mud? Earthquake nucleation and propagation through accretionary forearcs, *Geophys. Res. Lett.*, *38*, L18303, doi:10.1029/2011GL048552.

Faulkner, D., A. Lewis, and E. Rutter (2003), On the internal structure and mechanics of large strike-slip fault zones: Field observations of the Carboneras fault in southeastern Spain, *Tectonophysics*, *367*(3), 235–251.

Ferri, F., G. Di Toro, T. Hirose, and T. Shimamoto (2010), Evidence of thermal pressurization in high-velocity friction experiments on smectite-rich gouges, *Terra Nova*, *22*(5), 347–353, doi:10.1111/j.1365-3121.2010.00955.x.

Ferri, F., G. Di Toro, T. Hirose, R. Han, H. Noda, T. Shimamoto, M. Quaresimin, and N. de Rossi (2011), Low-to high-velocity frictional properties of the clay-rich gouges from the slipping zone of the 1963 Vaiont slide, northern Italy, *J. Geophys. Res.*, *116*, B09208, doi:10.1029/2011JB008338.

Fondriest, M., S. A. Smith, T. Candela, S. B. Nielsen, K. Mair, and G. Di Toro (2013), Mirror-like faults and power dissipation during earthquakes, *Geology*, *41*(11), 1175–1178.

French, M. E., H. Kitajima, J. S. Chester, F. M. Chester, and T. Hirose (2014), Displacement and dynamic weakening processes in smectite-rich gouge from the Central Deforming Zone of the San Andreas Fault, *J. Geophys. Res. Solid Earth*, *119*, 1777–1802, doi:10.1002/2013JB010757.

Gratier, J. P., F. Thouvenot, L. Jenatton, A. Tourette, M. L. Doan, and F. Renard (2013), Geological control of the partitioning between seismic and aseismic sliding behaviours in active faults: Evidence from the Western Alps, France, *Tectonophysics*, *600*, 226–242, doi:10.1016/j.tecto.2013.02.013.

Guerrieri, L., A. Blumetti, E. Esposito, A. Michetti, S. Porfido, L. Serva, E. Tondi, and E. Vittori (2009), Capable faulting, environmental effects and seismic landscape in the area affected by the 1997 Umbria–Marche (Central Italy) seismic sequence, *Tectonophysics*, *476*(1), 269–281.

Han, R., T. Shimamoto, T. Hirose, J. H. Ree, and J. Ando (2007), Ultralow friction of carbonate faults caused by thermal decomposition, *Science*, *316*(5826), 878–881.

Han, R., T. Hirose, T. Shimamoto, Y. Lee, and J. Ando (2011), Granular nanoparticles lubricate faults during seismic slip, *Geology*, *39*(6), 599–602.

Holdsworth, R. E. (2004), Weak faults—Rotten cores, *Science*, *303*(5655), 181–182, doi:10.1126/science.1092491.

Holdsworth, R., E. Van Diggelen, C. Spiers, J. De Bresser, R. Walker, and L. Bowen (2011), Fault rocks from the SAFOD core samples: Implications for weakening at shallow depths along the San Andreas Fault, California, *J. Struct. Geol.*, *33*(2), 132–144.

Hsu, Y.-J., M. Simons, J.-P. Avouac, J. Galetzka, K. Sieh, M. Chlieh, D. Natawidjaja, L. Prawirodirdjo, and Y. Bock (2006), Frictional afterslip following the 2005 Nias-Simeulue earthquake, Sumatra, *Science*, *312*(5782), 1921–1926, doi:10.1126/science.1126960.

Ide, S., A. Baltay, and G. C. Beroza (2011), Shallow dynamic overshoot and energetic deep rupture in the 2011 M_w 9.0, Tohoku-Oki earthquake, *Science*, *332*(6036), 1426–1429, doi:10.1126/science.1207020.

Ikari, M. J., D. M. Saffer, and C. Marone (2007), Effect of hydration state on the frictional properties of montmorillonite-based fault gouge, *J. Geophys. Res.*, *112*, B06423, doi:10.1029/2006JB004748.

Ikari, M. J., D. M. Saffer, and C. Marone (2009), Frictional and hydrologic properties of clay-rich fault gouge, *J. Geophys. Res.*, *114*, B05409, doi:10.1029/2008JB006089.

Ikari, M. J., C. Marone, and D. M. Saffer (2011), On the relation between fault strength and frictional stability, *Geology*, *39*(1), 83–86.

Lavecchia, G., P. Boncio, and N. Creati (2003), A lithospheric-scale seismogenic thrust in central Italy, *J. Geodyn.*, *36*(1–2), 79–94, doi:10.1016/S0264-3707(03)00040-1.

Lay, T., et al. (2005), The Great Sumatra-Andaman earthquake of 26 December 2004, *Science*, *308*(5725), 1127–1133, doi:10.1126/science.1112250.

Lockner, D. A., C. Morrow, D. Moore, and S. Hickman (2011), Low strength of deep San Andreas Fault gouge from SAFOD core, *Nature*, *472*(7341), 82–85.

Logan, J., C. Dengo, N. Higgs, and Z. Wang (1992), Fabrics of experimental fault zones: Their development and relationship to mechanical behavior, *Int. Geophys.*, *51*, 33–67.

Malagnini, L., F. P. Lucente, P. De Gori, and A. Akinci (2012), Control of pore fluid pressure diffusion on fault failure mode: Insights from the 2009 L'Aquila seismic sequence, *J. Geophys. Res.*, *117*, B05302, doi:10.1029/2011JB008911.

Marone, C. (1998), Laboratory-derived friction laws and their application to seismic faulting, *Annu. Rev. Earth Planet. Sci.*, *26*(1), 643–696.

Miller, S. A., C. Collettini, L. Chiaraluce, M. Cocco, M. Barchi, and B. J. Kaus (2004), Aftershocks driven by a high-pressure CO_2 source at depth, *Nature*, *427*(6976), 724–727.

Mizoguchi, K., T. Hirose, T. Shimamoto, and E. Fukuyama (2007), Reconstruction of seismic faulting by high-velocity friction experiments: An example of the 1995 Kobe earthquake, *Geophys. Res. Lett.*, *34*, L01308, doi:10.1029/2006GL027931.

Moore, D. E., and D. A. Lockner (2004), Crystallographic controls on the frictional behavior of dry and water-saturated sheet structure minerals, *J. Geophys. Res.*, *109*(B3), B03401, doi:10.1029/2003JB002582.

Moore, D. E., and D. A. Lockner (2007), Friction of the smectite clay montmorillonite: A review and interpretation of data, in *The Seismogenic Zone of Subduction Thrust Faults, MARGINS Theor. Exp. Earth Sci. Ser.*, vol. 2, edited by T. H. Dixon and J. C. Moore, pp. 317–345, Columbia Univ. Press, New York.

Moore, D. E., and D. A. Lockner (2011), Frictional strengths of talc-serpentine and talc-quartz mixtures, *J. Geophys. Res.*, *116*, B01403, doi:10.1029/2010JB007881.

Morrow, C. A., B. Radney, and J. D. Byerlee (1992), Frictional strength and the effective pressure law of montmorillonite and illite clays, in *Fault Mechanics and Transport Properties of Rocks*, edited by B. Evans, and T.-F. Wong, pp. 69–88, Academic, San Diego, Calif.

Morrow, C., J. Solum, S. Tembe, D. Lockner, and T. F. Wong (2007), Using drill cutting separates to estimate the strength of narrow shear zones at SAFOD, *Geophys. Res. Lett.*, *34*, L11301, doi:10.1029/2007GL029665.

Niemeijer, A., C. Marone, and D. Elsworth (2010), Fabric induced weakness of tectonic faults, *Geophys. Res. Lett.*, *37*, L03304, doi:10.1029/2009GL041689.

Rice, J. R., J. W. Rudnicki, and J. D. Platt (2014), Stability and localization of rapid shear in fluid-saturated fault gouge: 1. Linearized stability analysis, *J. Geophys. Res. Solid Earth*, *119*, 4311–4333.

Saffer, D. M., and C. Marone (2003), Comparison of smectite-and illite-rich gouge frictional properties: Application to the updip limit of the seismogenic zone along subduction megathrusts, *Earth Planet. Sci. Lett.*, *215*(1), 219–235.

Saffer, D. M., K. M. Frye, C. Marone, and K. Mair (2001), Laboratory results indicating complex and potentially unstable frictional behavior of smectite clay, *Geophys. Res. Lett.*, *28*(12), 2297–2300, doi:10.1029/2001GL012869.

Savage, H. M., P. J. Polissar, R. Sheppard, C. D. Rowe, and E. E. Brodsky (2014), Biomarkers heat up during earthquakes: New evidence of seismic slip in the rock record, *Geology*, *42*(2), 99–102.

Scholz, C. H. (1998), Earthquakes and friction laws, *Nature*, *391*(6662), 37–42.

Shimamoto, T., and A. Tsutsumi (1994), A new rotary-shear high-speed frictional testing machine: Its basic design and scope of research [in Japanese with English abstract], *J. Tectonic Res. Group Jpn*, *39*, 65–78.

Sibson, R. H. (1975), Generation of pseudotachylyte by ancient seismic faulting, *Geophys. J. Int.*, *43*(3), 775–794, doi:10.1111/j.1365-246X.1975.tb06195.x.

Sibson, R. H. (1981), Fluid flow accompanying faulting: Field evidence and models, in *Earthquake Prediction*, pp. 593–603, AGU, Washington, D. C.

Siman-Tov, S., E. Aharonov, A. Sagy, and S. Emmanuel (2013), Nanograins form carbonate fault mirrors, *Geology*, *41*(6), 703–706.

Smith, S., G. Di Toro, S. Kim, J. H. Ree, S. Nielsen, A. Billi, and R. Spiess (2013), Coseismic recrystallization during shallow earthquake slip, *Geology*, *41*(1), 63–66.

Sone, H., T. Shimamoto, and D. E. Moore (2012), Frictional properties of saponite-rich gouge from a serpentinite-bearing fault zone along the Gokasho-Arashima Tectonic Line, central Japan, *J. Struct. Geol.*, *38*, 172–182.

Tembe, S., D. A. Lockner, and T. F. Wong (2010), Effect of clay content and mineralogy on frictional sliding behavior of simulated gouges: Binary and ternary mixtures of quartz, illite, and montmorillonite, *J. Geophys. Res.*, *115*, B03416, doi:10.1029/2009JB006383.

Tesei, T., C. Collettini, B. M. Carpenter, C. Viti, and C. Marone (2012), Frictional strength and healing behavior of phyllosilicate-rich faults, *J. Geophys. Res.*, *117*, B09402, doi:10.1029/2012JB009204.

Tesei, T., C. Collettini, C. Viti, and M. R. Barchi (2013), Fault architecture and deformation mechanisms in exhumed analogues of seismogenic carbonate-bearing thrusts, *J. Struct. Geol.*, *55*, 167–181.

Ujiie, K., and A. Tsutsumi (2010), High-velocity frictional properties of clay-rich fault gouge in a megasplay fault zone, Nankai subduction zone, *Geophys. Res. Lett.*, *37*, L24310, doi:10.1029/2010GL046002.

Ujiie, K., A. Tsutsumi, and J. Kameda (2011), Reproduction of thermal pressurization and fluidization of clay-rich fault gouges by high-velocity friction experiments and implications for seismic slip in natural faults, *Geol. Soc., London Spec. Publ.*, *359*(1), 267–285.

Ujiie, K., et al. (2013), Low coseismic shear stress on the Tohoku-Oki megathrust determined from laboratory experiments, *Science*, *342*(6163), 1211–1214, doi:10.1126/science.1243485.

Ventura, G., and R. Di Giovambattista (2013), Fluid pressure, stress field and propagation style of coalescing thrusts from the analysis of the 20 May 2012 M_L 5.9 Emilia earthquake (Northern Apennines, Italy), *Terra Nova*, *25*(1), 72–78, doi:10.1111/ter.12007.

Verberne, B. A., C. He, and C. J. Spiers (2010), Frictional properties of sedimentary rocks and natural fault gouge from the Longmen Shan fault zone, Sichuan, China, *Bull. Seismol. Soc. Am.*, *100*(5B), 2767–2790.

Verberne, B. A., C. J. Spiers, A. R. Niemeijer, J. H. P. De Bresser, D. A. M. De Winter, and O. Plümper (2014), Frictional properties and microstructure of calcite-rich fault gouges sheared at sub-seismic sliding velocities, *Pure Appl. Geophys.*, *171*(10), 2617–2640, doi:10.1007/s00024-013-0760-0.

Violay, M., S. Nielsen, E. Spagnuolo, D. Cinti, G. Di Toro, and G. Di Stefano (2013), Pore fluid in experimental calcite-bearing faults: Abrupt weakening and geochemical signature of co-seismic processes, *Earth Planet. Sci. Lett.*, *361*, 74–84, doi:10.1016/j.epsl.2012.11.021.

Vittori, E., G. Deiana, E. Esposito, L. Ferreli, L. Marchegiani, G. Mastrolorenzo, A. Michetti, S. Porfido, L. Serva, and A. Simonelli (2000), Ground effects and surface faulting in the September–October 1997 Umbria–Marche (Central Italy) seismic sequence, *J. Geodyn.*, *29*(3), 535–564.

Vrolijk, P., and B. A. van der Pluijm (1999), Clay gouge, *J. Struct. Geol.*, *21*(8), 1039–1048.

Wu, F. T., L. Blatter, and H. Roberson (1975), Clay gouges in the San Andreas Fault system and their possible implications, *Pure Appl. Geophys.*, *113*(1), 87–95, doi:10.1007/BF01592901.

Yamaguchi, A., A. Sakaguchi, T. Sakamoto, K. Iijima, J. Kameda, G. Kimura, K. Ujiie, F. M. Chester, O. Fabbri, and D. Goldsby (2011), Progressive illitization in fault gouge caused by seismic slip propagation along a megasplay fault in the Nankai Trough, *Geology*, *39*(11), 995–998.